

# Thermo-Optic Beam Scanner Employing Silicon Photonic Crystal Slow-Light Waveguides

Takemasa Tamanuki, Hiroyuki Ito, and Toshihiko Baba , *Member, IEEE, Member, OSA*

(Invited Paper)

**Abstract**—Optical beam scanning is a widely utilized function in optical systems and a compact nonmechanical solid-state device has long been anticipated. Here, we have studied such a device consisting of photonic crystal slow-light waveguides and switch trees, fabricated by a Si photonics process, employing a bespoke prism lens for beam collimation. Further in this study, we particularly demonstrated the operation of the device only by the thermo-optic (TO) tuning of its components, at a fixed wavelength of light. A spot beam of  $\sim 0.1^\circ$  divergence, was scanned in two dimensions, in the angular range of  $40^\circ \times 8.8^\circ$  and average power consumption of  $< 0.7$  W. Neglecting some disordered beams caused by the non-uniformity of the fabricated device, the estimated number of resolution points was  $400 \times 32 = 12,800$ , which required a significant effort in the device fabrication and calibration, utilizing optical-phased arrays, if the same performance was targeted.

**Index Terms**—Beam scanner, solid-state, silicon photonics, photonic crystal, slow-light.

## I. INTRODUCTION

**A**N OPTICAL beam scanner is employed for laser processing, laser microscopy, laser display and projection, printing, decoding, three-dimensional (3D) profiling, motion capturing, identification, optical coherence tomography, light detection and ranging (LiDAR), etc. Conventional commercial beam scanners all exploit mechanics, such as Galvano and polygon mirrors. Their technology is well-established while their large sizes and power consumption, less-flexible motion due to their moments of inertia, and instability against vibrations are their constraints. A micro-electro-mechanical system (MEMS) mirror is a practical solution for the construction of a miniature system, although other constraints remain. A complete nonmechanical solid-state beam scanner has been anticipated for a long time, although it is still a challenge to fabricate one.

Table I compares one-dimensional (1D) beam scanning devices that have been studied so far. Liquid crystal [1] and

electro-optic (EO)/acousto-optic (AO) crystals [2] are beneficial as bulk beam scanners, although their high operation voltages, temperature sensitivity, and/or small steering angle hamper their application. Si photonics and compound semiconductor devices are attractive because they can be integrated with other functional optical components. Particularly, optical phased arrays (OPAs) have been developed extensively in this decade [3]–[9]. OPAs are attractive if a large number of optical antennas, each consisting of a miniature diffraction grating, is integrated with a small spacing close to the optical wavelength,  $\lambda$ , to avoid ghost beams; light is uniformly distributed to them with a small optical loss; and an arbitrary wavefront is synthesized by precisely controlling the optical phases of all the antennas via, for example, the thermo-optic (TO) effect, with reasonably low power consumption. However, all the approaches are still challenging. Waveguide gratings are more common devices that produce narrow beams and steer it by sweeping  $\lambda$  [10]. However, its range for a reasonable sweep is small. To overcome these constraints, a slow-light waveguide [11], exhibiting a guided mode, with a large group index,  $n_g$ , can be employed. In general,  $n_g$  is given as  $c(d\beta/d\omega)$ , where  $c$ ,  $\beta$ , and  $\omega$ , are the vacuum-light velocity, modal propagation constant, and frequency. The large  $n_g$  is equivalent to a large angular dispersion when the waveguide mode is converted to a free-space beam via grating [12]. Actually, slow-light waveguide grating increases the steering range by 5–10 times that of simple gratings for the same  $\lambda$  sweep. This also allows the utilization of the TO tuning of the refractive index of the waveguide, instead of the  $\lambda$  sweep, to steer the beam, thus simplifying the total system.

Table II shows the two-dimensional (2D) beam scanning schemes with respect to Si photonic devices. 2D OPAs increase the attraction but simultaneously with the challenges of OPAs [4]. Therefore, 1D OPAs, consisting of waveguide gratings, have been employed as a practical solution [5]. In this scheme, the  $\lambda$  sweep is necessary, and therefore, the steering range in the direction along the waveguides is limited. If slow-light waveguide gratings are employed in 1D OPAs, a wide steering range would be obtained in 2D and the full operation by the TO tuning without the  $\lambda$  sweep would be available. However, a flat slow-light spectrum suitable for this purpose has only been obtained in a lattice-shifted photonic crystal waveguide (LSPCW) [13], [14] whose width, including the photonic crystal claddings, is wider than  $10\lambda$ . Therefore, ghost beams cannot be suppressed if OPA is constructed by this waveguide. Another scheme, employing

Manuscript received July 15, 2020; revised September 16, 2020; accepted October 17, 2020. Date of publication October 20, 2020; date of current version February 16, 2021. This work was funded by the Accelerated Innovation Research Initiative Turning Top Science and Ideas into High-Impact Values (ACCEL) and by the Japan Science and Technology Agency (JST) under Grant JPMJAC1603. (Corresponding author: Toshihiko Baba.)

The authors are with the Department of Electrical and Computer Engineering, Yokohama National University, Yokohama 240-8501, Japan (e-mail: tamanuki-takemasa-jd@ynu.ac.jp; ito-hiroyuki-tw@ynu.ac.jp; baba@ynu.ac.jp).

Color versions of one or more of the figures in this article are available online at <https://ieeexplore.ieee.org>.

Digital Object Identifier 10.1109/JLT.2020.3032519

TABLE I  
NONMECHANICAL SOLID-STATE BEAM SCANNERS

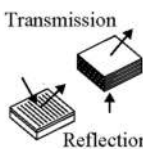
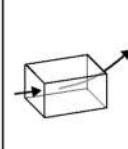
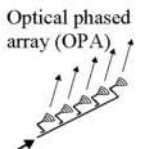
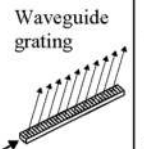
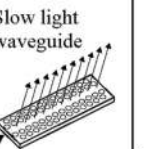
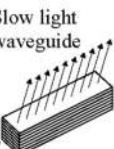
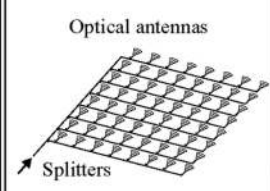
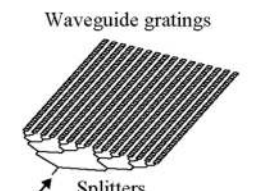
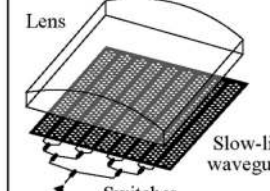
Material	Liquid Crystal	EO/AO Crystal	Si Photonics			Compound Semiconductor
Type	Transmission  Reflection		Optical phased array (OPA) 	Waveguide grating 	Slow light waveguide 	Slow light waveguide 
Pros	Quality beam High resolution	Simple Quality beam High speed	Integration Flexible steering by electronics	Integration Simple Narrow beam	Integration Large angle High resolution TO scanning	Large angle High resolution High power output
Cons	Bulky High voltage Temperature sensitive	Bulky High voltage Small angle	Lossy Side lobe Complicated Power consuming	Small angle Side lobe $\lambda$ sweep necessary	Lossy Side lobe	$\lambda$ sweep necessary

TABLE II  
NONMECHANICAL 2D BEAM-SCANNING DEVICES IN SI PHOTONICS. A SIMPLE CYLINDRICAL LENS IS ILLUSTRATED IN THE THIRD TYPE, ALTHOUGH A BESPOKE PRISM LENS WAS REQUIRED

Type	2D OPA	Waveguide grating + 1D OPA	Switching of slow light waveguide + collimator lens
Structure	Optical antennas  Splitters	Waveguide gratings  Splitters	Lens  Slow-light waveguides Switches
Pros	Flat Flexible beam steering	Flat Flexible beam steering	Wide angle, high resolution Simple control Power saving Complete TO control
Cons	Trade-off between angle and resolution Complicated Power consuming	Small angle along the waveguide Complicated Power consuming $\lambda$ tuning necessary	Thick device Discrete steering in the direction across the waveguide

slow-light waveguides, involves the selection of one waveguide from the arrayed waveguides, for light incidence. Here, because light is diverged in the lateral direction, a collimator lens is utilized to form the spot beam. Thereafter, the light is steered in the lateral direction when the position of selected waveguide is offset from the center of the lens [15]. In this scheme, a thick system resulting from the lens and its focal length and a discrete lateral beam-steering may be the drawbacks.

We have proposed this third scheme, and so far developed a device consisting of LSPCWs and switch trees, which are all integrated by the Si photonics complementary-metal oxide-semiconductor (CMOS) process, as well as a bespoke collimator lens [16]. We demonstrated the 2D scanning of a spot beam of  $\sim 0.15^\circ$  divergence in the angular range of  $40^\circ \times 4.4^\circ$  with an estimated resolution point,  $266 \times 16$ , by the combination of the  $\lambda$  sweep and TO waveguide switching. In this paper, we report the full TO operation of this device without employing the  $\lambda$  sweep. The detail of the device is presented in Section II, the

beam-scanning characteristics in Section III, and the evaluation of the response speed is shown in Section IV.

## II. DEVICE

The structure and fabrication processes of the Si photonics chip were according those in Ref. [16]. We employed a 200-mm-diameter silicon-on-insulator (SOI) with a 210-nm-thick Si layer and the CMOS process with a KrF excimer laser stepper at  $\lambda = 248$  nm and phase-shift masks, for which the minimum feature size was  $< 130$  nm.

Fig. 1(a) shows the schematic of a  $\text{SiO}_2$ -clad Si LSPCW consisting of a single-line-defect core, sandwiched by photonic crystal claddings, and Fig. 1(b) shows the magnified scanning electron micrograph (SEM) of fabricated LSPCW with shallow-etched gratings. The hole diameter and pitch of the triangular-lattice photonic crystal were 192 and 394 nm, respectively. The above generic process was enough to fabricate these holes. The

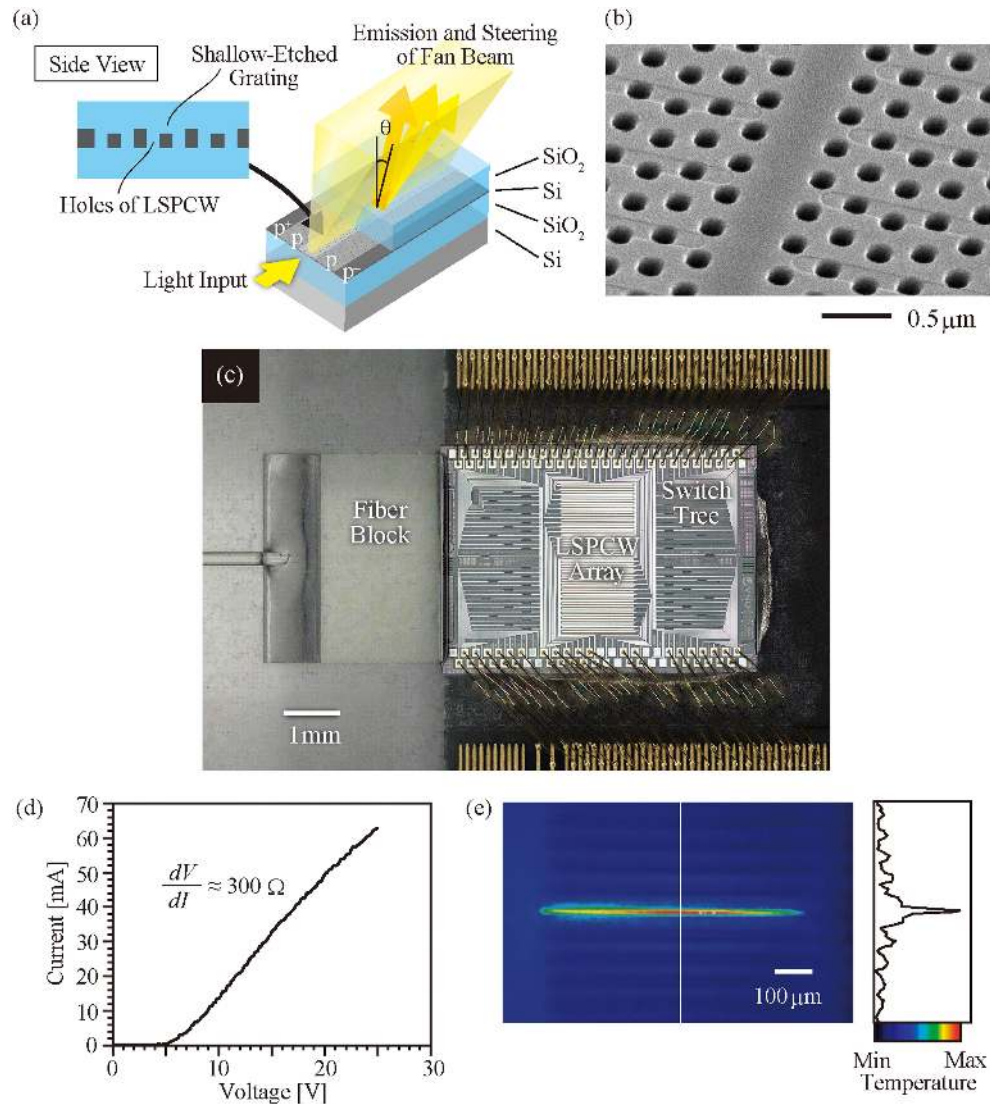


Fig. 1. Fabricated Si photonics chip. (a) Schematic of the beam steering device, consisting of  $\text{SiO}_2$ -clad and p-i-p-doped Si LSPCW with shallow-etched gratings. (b) Perspective SEM view of LSPCW with the grating, taken after removing the top  $\text{SiO}_2$  cladding. (c) Top-view of the Si photonics chip die-bonded on an Al block and wire-bonded to a printed circuit board with an attached input fiber. (d) Electrical characteristics of the p-i-p doped LSPCW. (e) Thermal image of LSPCW heated at  $P = 1.3$  W, which was observed by microscopic thermography.

lattice-shift of 95 nm was added to the third rows of the holes, targeting the slow-light transmission window,  $\Delta\lambda = 23$  nm, thus exhibiting a nearly constant  $n_g$  of  $\sim 18$ , at  $\lambda$  of around 1,550 nm. The gratings with a depth of  $\sim 10$  nm and a pitch that is twice larger were formed so that the edge of each grating was located between the two holes on the first rows. In finite-difference time-domain simulations, such gratings exhibited an emission rate of 100 dB/cm and a 60% upward emission (40% downward), regardless of the direction of the light propagation. Further, LSPCW was p-i-p-doped to heat the undoped core selectively when the electric current flowed across the waveguide [17]. The target concentration of p-doping was  $1.05 \times 10^{18} \text{ cm}^{-3}$ . The width of the i region was set at  $1.5 \mu\text{m}$  to ensure that the free-carrier absorption loss in the slow-light mode was comparable to the scattering loss of the fabricated LSPCW without doping, i.e., 10–30 dB/cm, and much lower than the target emission rate. The length of LSPCW was 1.23 mm.

The complete view of the fabricated chip is shown in Fig. 1(c), where 32 LSPCWs were integrated with a  $80 \mu\text{m}$  pitch at the center of the chip. This pitch included a large margin, and it can ideally be reduced to  $20 \mu\text{m}$ , considering the width of the LSPCW ( $8.2 \mu\text{m}$  in total for 12 rows of holes on each side of the waveguide channel) as well as that of Al wires and contacts. Therefore, 128 LSPCWs can be integrated maximally without margin for the same footprint. The chip was die-bonded to an Al block and wire-bonded to a printed circuit board. An external single-mode laser light of transverse-electric polarization was coupled to a Si inverse-tapered spot-size converter at a facet via a high  $\Delta$  core-shrunk polarization-maintaining fiber, which was directly attached to the facet by an ultraviolet curing resin. The light was launched on one of the 32 LSPCWs after passing through either left or right side of a  $1 \times 32$  Si-wire waveguide switch-tree. Both ends of LSPCWs were connected to the switch-tree via low loss-tapered junctions [18]. The switch-tree

was composed of  $1 \times 2$  Mach-Zehnder switches, each driven by a  $100 \mu\text{m}$  long TiN TO heater. One of the two switch-trees contained 31 switches, and two switch-trees were switched so that the direction of the light propagation in LSPCWs was changed in order to double the angular-range of beam scanning. Therefore, the total number of TO heaters was 95 (32 for LSPCWs and 63 for the switches). The size of the chip was  $5.5 \text{ mm} \times 3.95 \text{ mm}$ . This lateral size was not determined by LSPCWs and the switches; it was determined by the footprint of the electric pads. Employing flip-chip bonding, we could reduce the chip-size to  $3.5 \text{ mm} \times 3.5 \text{ mm}$ . The  $\pi$ -phase-shift power consumption of each switch was 15 mW. Only six switches were operated simultaneously for the selection of one LSPCW and one direction of the light propagation. Although excess power was required to compensate for the initial phase-offset in each switch, the total power consumption of the switch was no higher than 200 mW, and the average value was  $< 100 \text{ mW}$ .

Fig. 1(d) shows a typical current-voltage characteristic of the p-i-p heater. Because of the partial reverse bias in this junction, the threshold behavior appeared. The series resistance above the threshold was  $300 \Omega$ . The operation was stable at a voltage of  $V < 28 \text{ V}$  or a heating power  $P < 2.1 \text{ W}$ . Fig. 1(e) shows a thermal image of LSPCWs, taken by microscopic thermography (ViewOhre IMAGING, MCR32), when  $P$  of 1.3 W was injected into LSPCW in a test element group (TEG) chip. Although the absolute temperature was not precisely evaluated because of the uncertain radiation coefficients of materials, we confirmed the well-concentrated heating around LSPCW; the lateral heat diffusion was distributed within  $\sim 20 \mu\text{m}$ , which was narrower than the  $40 \mu\text{m}$  of the TiN heater of the switch that was buried in the  $\text{SiO}_2$ -cladding [16]. Because any one of the LSPCWs is heated during the beam steering, this heat diffusion does not matter, even when the LSPCW pitch is extremely reduced, as mentioned above.

The collimator lens above the chip was also mounted on the printed circuit board, as shown in Fig. 2(a). Light emitted from LSPCW formed a fan beam, and that at any beam angle  $\theta$  must be converted into a spot-beam by this lens. For this purpose, a simple cylindrical lens does not work; it works only at a certain  $\theta$  because the distance between the chip and lens and the focal length of the lens vary inversely with  $\theta$ . Additionally, the light emitted from LSPCW disappeared at  $\theta = 0^\circ$  under Bragg's condition, thereby resulting in the blind angular range of beam scanning. To solve these challenges, we developed a symmetric prism lens, as shown in Fig. 2(a). The detail of its shape and principle are contained in Ref. [19]. The lens was designed to uniformly convert the fan beam of  $\theta = 10^\circ\text{--}30^\circ$  to a spot beam of  $< 0.1^\circ$  divergence. An almost similar collimation was maintained even when LSPCW was slightly offset against the lens. Therefore, it could be employed for lateral beam-steering in the  $\phi$  direction. Furthermore, the refraction at the prism converted the range of  $\theta = 10^\circ\text{--}30^\circ$  to  $\theta' = 0^\circ\text{--}20^\circ$ , which eliminated the blind range and obtained continuous beam-scanning from  $-20^\circ$  to  $+20^\circ$ , which was available by switching the direction of the light propagation. We fabricated this lens with pedestals by acrylic cutting and fix it to the Al block.

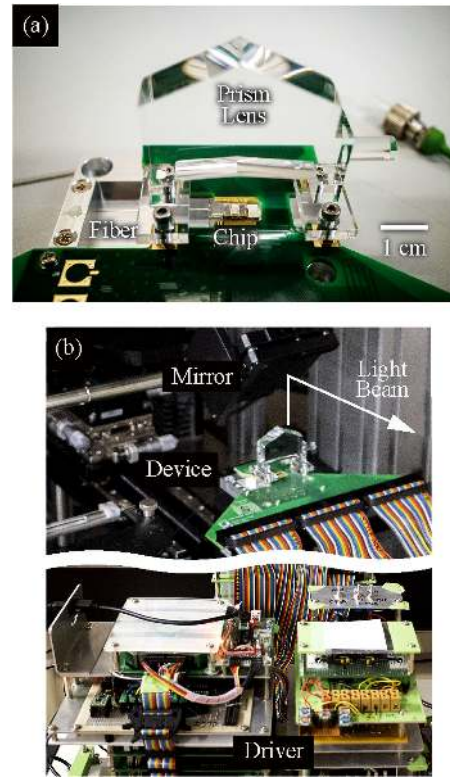


Fig. 2. (a) Total device view of the chip on board with a prism lens loaded. (d) Experimental setup.

Fig. 2(b) shows the experimental setup for the evaluation of the beam scanning. The emitted and collimated beams were first observed by the microscope, which was equipped with optics for the far-field pattern (FFP) observation and  $1280 \times 1,024$  pixels InGaAs camera (resolution,  $0.0288^\circ$ ), that was placed above the device. When the free-space beam was observed, the beam was reflected by a  $45^\circ$  mirror. The TO heaters were driven by op-amps controlled by a personal computer or field-programmable gate array, through digital-analog converters. The onset time of this circuit was  $10 \mu\text{s}$ .

### III. BEAM SCANNING

In this paper, we did not exhibit the  $\lambda$ -swept beam scanning of the device because its details are already contained in Ref. [16]. The 1D TO beam scanning characteristics are summarized in Fig. 3. The beam was first evaluated with the FFP microscope, where  $\lambda$  was fixed at  $1.58 \mu\text{m}$ , and the light was launched on a LSPCW close to the center by controlling the switches. When the LSPCW was heated, a slow drift of the beam, in which the saturation time was longer than 3 s, was observed. Therefore, we evaluated the spot after setting  $P$  and an adequate waiting time. Figs. 3(a) and (b) show some spot patterns and their profiles when  $P$  was changed in the range of 0–1.2 W and when the direction of light propagation was switched. Fig. 3(c) is the magnified image of one spot, indicated by the arrow in Fig. 3(a). Figs. 3(d) and (e) summarize  $\theta'$ s above the prism lens, and the beam divergence,  $\delta\theta'$  and  $\delta\phi$  (full-width at half

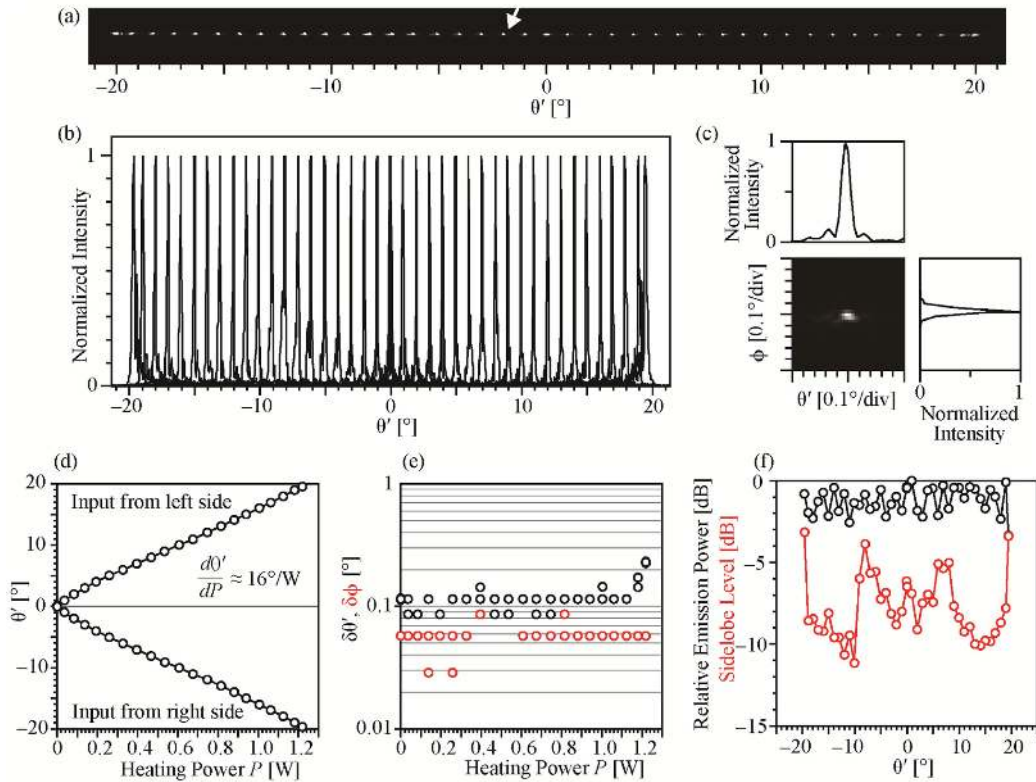


Fig. 3. Observation of 1D optical beam steering using TO effect. (a) FFP of steered beam at  $\lambda = 1.58 \mu\text{m}$ . (b) Normalized profile of the beam in (a). (c) Magnified FFP image and profiles of the beam indicated by an arrow in (a). (d) Steering angle above the prism lens,  $\theta'$ , for heating power  $P$ , where  $\theta'$  was changed from minus to plus by switching the orientation of light propagation in the LSPCW. (e) Beam divergence for heating power. (f) Relative emission power and sidelobe level measured for  $\theta'$ .

maximum (FWHM)), as functions of  $P$ , respectively. The beam was steered from  $-20^\circ$  to  $+20^\circ$  (the total steering range,  $\Delta\theta' = 40^\circ$ ) with a power dependence of  $d\theta'/dP \approx 1.6^\circ/\text{W}$ . Considering the temperature-dependent refractive indices of materials, the highest temperature increase for the maximum heating power was estimated to be 300 K. The range  $\theta' = 0^\circ$ – $20^\circ$  in one direction of light propagation was determined by the range of  $\theta$  and the prism angle. The former was governed by the photonic band-edge without heating, and the crosspoint of the  $\text{SiO}_2$  light line and the waveguide band shifted with heating; thus, it was slightly expanded by the heating, as compared with the  $\lambda$ -swept scanning. The calculation of the photonic band suggested that  $\theta = 0^\circ$ – $32^\circ$  was possible [17], although the emission disappeared at  $\theta = 0^\circ$ , as already mentioned, and the beam divergence and disordering increased gradually when  $\theta$  approached  $0^\circ$ . Therefore, we set  $\lambda$  at  $1.58 \mu\text{m}$ , which was slightly shorter than the band-edge wavelength, and employed  $\theta = 10^\circ$ – $30^\circ$  to obtain  $\theta' = 0^\circ$ – $20^\circ$ . However,  $\theta' = 0^\circ$ – $27^\circ$  from  $\theta = 5^\circ$ – $32^\circ$  and  $\Delta\theta' = 54^\circ$  are obtainable potentially by redesigning the prism lens.

All the spots were well-collimated but the profile in Fig. 3(b) at  $\theta' = 0^\circ$  looks to be a slightly wider than the others. It was due to the split peaks at  $P = 0 \text{ W}$  before and after the switching of directions. Their difference was  $\sim 0.1^\circ$ . As the guided mode was mainly emitted near the input end of the waveguide, the main emission area was shifted by the length of LSPCW (1.23 mm) before and after the switching. The  $0.1^\circ$  difference suggested slow nonuniformity over the chip. The angular dispersion  $d\theta'/d\lambda$

was  $0.9^\circ/\text{nm}$ , and the calculated dependence of the photonic band wavelength on the hole diameter of the photonic crystal,  $d\lambda/d(2r)$ , was 1.6. Therefore, the above  $0.1^\circ$  difference corresponds to a 0.07 nm error in  $2r$ . Such a small error or its equivalent in the thickness of the Si layer could occur, even accounting for an average around each area. It could be suppressed by a more advanced CMOS process with 300-mm-diameter SOI and ArF exposure. Actually, we could fit the split peaks by shifting  $\lambda$  by  $\sim 0.04 \text{ nm}$  on the long wavelength side. Figs. 3(b) and (e) also show the increased beam divergence and disordered profiles, at  $\theta' = \pm 20^\circ$ , of the highest  $P$ . Because it corresponds to the light-line condition with almost a constant  $n_g$ , such disordering was not generally observed in the  $\lambda$ -swept scanning. It was caused by a gradual drop in temperature near both ends of LSPCW, where the strongest emission occurs. We confirmed in a supplemental experiment for the TEG chip that the increased beam divergence disappeared when 100- $\mu\text{m}$ -long non-emissive regions without gratings were arranged near the ends of LSPCW.

The average beam divergence  $\delta\theta'$  was  $0.1^\circ$  and the number of resolution points evaluated from  $\Delta\theta'/\delta\theta$  was 400. These values were better than the  $\lambda$ -swept beam scanning in Ref. [16]. But it was not owing to the TO tuning but just a better chip selected and used in this study. They were maintained when another one of the 32 LSPCWs was selected for the  $\phi$ -directional beam steering, although it was difficult to evaluate all the spots separately under the same conditions because of the slow thermal drift. Operating all LSPCWs, we confirmed that the  $\phi$ -directional steering range

$\Delta\phi$  was  $8.8^\circ$ . Neglecting the irregular points, which exhibited the disordered profiles, we roughly estimated the number of resolution points in the 2D scanning to be  $400 \times 32 = 12,800$ . As the resolution points in the  $\phi$  direction is simply determined by the number of LSPCWs, it will be increased up to 128 for the maximum filling of the LSPCWs.

Fig. 3(f) shows the peak intensity fluctuations and side lobe level. The fluctuation was caused by the interference between upward and downward emission inside the device. Further optimization is necessary for the grating structure to enhance the upward emission ratio. The side lobe level ranged from  $-11.5$  dB to  $-3.7$  dB of the peak intensity, except at  $\pm 20^\circ$  close to the band-edge condition. The light emission decays exponentially along the LSPCW, for which the corresponding FFP is Lorentzian with no side lobes when the LSPCW is sufficiently long. Therefore, the observed side lobe was caused by the nonuniform local scattering. It was particularly enhanced by voids inside the  $\text{SiO}_2$  cladding; we observed such voids formed inside or above the holes of LSPCW. Their size and position were sensitive to the  $\text{SiO}_2$  deposition process, and large voids severely disordered the beam and increased the side lobe level. Their size was minimized in the present device, but we expect a lower side lobe level by completely eliminating the voids.

#### IV. FREE SPACE BEAM TRANSMISSION

Thereafter, we tested the free-space beam transmission. Neglecting the intensity fluctuation in Fig. 3(f), the insertion loss from the fiber to the free-space beam was estimated to be 13 dB, at the lowest, including (i) 3 dB for the fiber coupling, (ii) 1.7 dB for the propagation loss of the Si wire, (iii) 1.8 dB for the switch tree, (iv) 0.5 dB for the Si wire and LSPCW coupling, (v) 2 dB for the propagation loss of LSPCW, (vi) 2 dB for downward emission, and (vii) 2 dB for the light extraction and collimation. Regarding (i)–(iv), we expected the reduction by  $> 4.5$  dB by employing a more advanced CMOS process and design, which resulted in a total loss of  $< 9$  dB. Regarding (v)–(vii), more designs for optimization may be required. Only the essential loss was expected to be the absorption loss of  $< 2$  dB due to the p-i-p doping.

Fig. 4 shows the observation of the continuous 2D scanning of the free-space beam. Here, a semi-transparent screen was placed in front of the device at a 90 cm distance, and the spot profile was observed by an InGaAs camera from behind. To avoid the thermal drift, which depended on  $P$ , we observed the dynamic raster scanning at a duration of 2–10 s for each line (1–5 min for 32 lines in a frame), so that the camera could capture it almost clearly. Fig. 4(b) shows the image, produced by overlaying the taken video frames. From this, the scanning range,  $\Delta\theta = 40^\circ$  and  $\Delta\phi = 8.8^\circ$ , were confirmed. The center gap was caused by the aforementioned split peaks at  $P = 0$  W. It could be compensated for by optimizing  $\lambda$  and calibrating the range of  $P$  for each LSPCW. The maximum and average power consumption were 1.2 and 0.6 W, respectively. Even adding that for the switches, the average power consumption was no higher than 0.7 W.

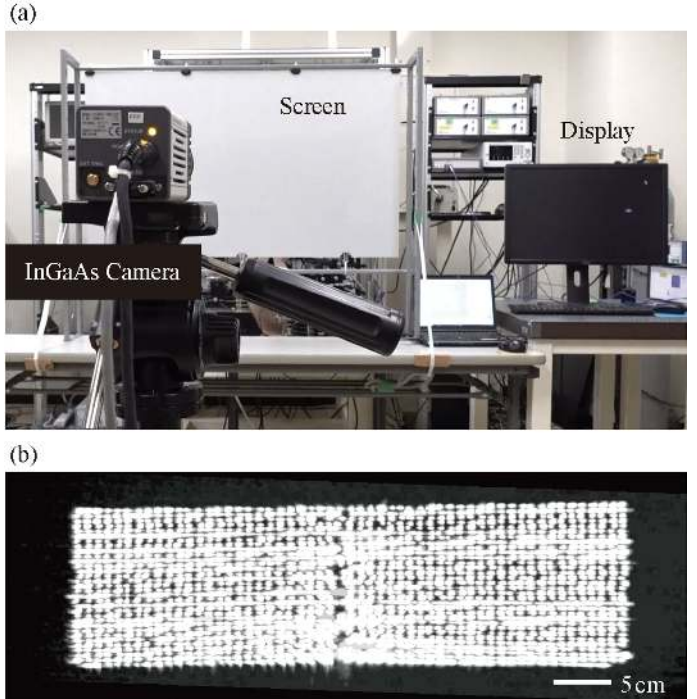


Fig. 4. Demonstration of dynamic 2D beam steering. (a) Experimental setup. Device was placed on the back side of the screen with a distance of 90 cm. The beam emitted and irradiated on the screen was observed by InGaAs camera on the front. (b) Overlaid spots on the screen, which were taken from video frames of real time beam steering.

#### V. RESPONSE SPEED

To evaluate the response speed, we launched light on one LSPCW and repeated the 1D scanning with a sinusoidal voltage from a function generator at the frequency  $f$  after amplification. A large swing, 6.7–22.3 V, and a small swing, 14.3–15.7 V, demonstrated almost the same frequency responses after the normalization. Therefore, only the results for the large swing are shown in Fig. 5. The difference between those at  $f = 1$  and 10 Hz was due to the slow drift. At  $f > 10$  Hz, the response became almost flat up to 10 kHz, and thereafter dropped to half at  $f_c = 70$  kHz. Assuming the exponential thermal response, the corresponding time constant is  $2.3 \mu\text{s}$  and the 90% onset time is  $5.0 \mu\text{s}$ . Adding the onset time of the utilized driver circuit, the total onset time became  $15 \mu\text{s}$ . This potentially achieves the scanning of the above resolution points within 0.192 s, thus implying a frame-rate of 5.2 fps (10  $\mu\text{s}$  order onset time of the MZ switches was negligible in the frame). If the response of the driver circuit is improved so that its onset time also becomes negligible, the frame-rate will be  $> 15$  fps. Regarding the device response, we previously measured  $f_c \approx 100$  kHz in a similar p-i-p-doped LSPCW [17], for which the onset time of  $3.5 \mu\text{s}$  and a frame-rate of  $> 20$  fps were expected. In that experiment, the chip was not die-bonded and the electrical contact was conducted by a probe instead of the wire-bonding. This suggested that there were still rooms for optimization in the chip and the surrounding elements toward high-speed thermal response.

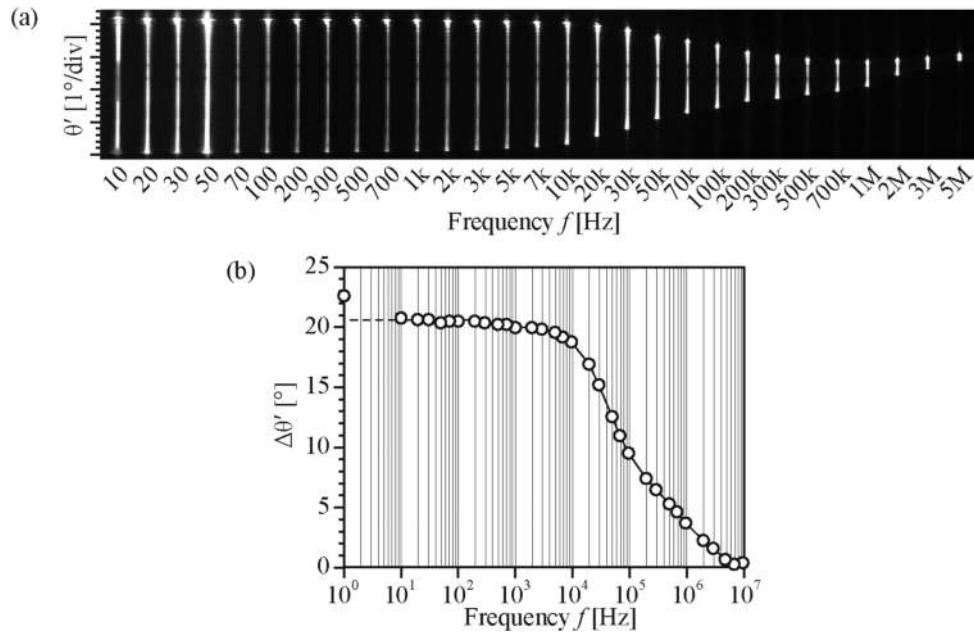


Fig. 5. Response speed. (a) FFP of the continuously steered beam, at different frequencies. (b) Frequency response, evaluated from (a).

## VI. DISCUSSION

Let us compare the TO beam steering with  $\lambda$ -swept one. The beam quality is almost the same. Important advantages of the TO steering are that it allows to use a simpler laser source and achieves a high speed. A standard distributed feedback laser diode can be used at a fixed  $\lambda$ , although  $\lambda$  must be tuned to the photonic band-edge in advance. Once it is tuned, the relation between  $\lambda$  and band-edge does not change so severely with the environmental temperature when the laser and device are contained on the same carrier because the temperature dependence of such singlemode lasers and Si photonics components are similar. Regarding the speed, it is difficult to obtain  $>10$  kHz order response with maintaining high coherence in  $\lambda$ -swept lasers. Using the TO eliminates these constraints with a reasonable average power consumption of 0.7 W. A concern may be the instability for high temperature operation. For highest  $\Delta T \approx 300$  K in this type of device, we observed no degradations for 50 h continuous operation. The  $\Delta\theta$  can be extended to  $\pm 27^\circ$  potentially, for which the corresponding  $\Delta T$  is estimated to be 400 K. We also tested at this temperature and confirmed the similar stability. Therefore, this  $\Delta\theta$  will become available by improving the beam quality.

Next, we compare the device with OPAs. The full flatness is a significant appeal point of OPAs, and our device with the prism lens lost it. The size and focal length of this lens can be reduced in analogous shape but the uniform collimation for different  $\theta$  is degraded gradually. Further optimization of the design is necessary to moderately suppress this degradation. We wonder if the prism lens can be replaced with some full-flat optics such as metalenses. But even with the current lens, the total space required is no larger than  $40 \text{ mm} \times 40 \text{ mm} \times 10 \text{ mm}$ , which is already compact as a beam scanner. A merit of using the lens is a beam aperture simply enlarged by the lens. The

large aperture is crucial particularly when the device is used for the reception of returned light in LiDAR. In OPAs, it is only possible by enlarging the device size on a chip, resulting in a high cost. The post control of the beam profile is another advantage of OPAs, although it needs the complicated phase tuning. The beam quality of our device is simply determined by the device quality. But we obtained  $\delta\theta = 0.1^\circ$  and the large number of resolution points in the device fabricated by generic CMOS process. We consider it to be attributed to the simple grating structure, and expect the significant improvement when a more advanced CMOS process is employed and the voids, as mentioned in Section III, are completely eliminated. Regarding the speed, our device is superior to the combination of the  $\lambda$ -sweep and 1D OPA. Comparable or even higher speeds may be achievable in 2D OPAs by employing the TO effect or much faster carrier plasma dispersion for the phase control, while 2D OPAs are not suitable for the reception in LiDAR because of a low filling ratio of optical antennas in an effective chip area. The insertion loss is a common problem for these devices and most Si photonics devices as well. But, as their major components depend on the fabrication process, they will be reduced by further optimizations.

Finally, we discuss a point to be noted when our device is applied to frequency-modulated continuous-wave (FMCW) LiDAR. Most commercial LiDARs employ time-of-flight (TOF) method, in which the range information is acquired from the delay of round-trip optical pulses. However, it is difficult to apply this type to Si photonics, because of the two-photon absorption problem for watt-class high-power pulses in TOF LiDARs. The FMCW LiDAR does not need such high powers but a complicated photonic circuit instead, which is suitable for Si photonics. In FMCW LiDARs, frequency-swept light is used for ranging, and this results in an angular shift of the beam in our device. As the angular dispersion of our device was  $0.9^\circ/\text{nm}$

( $= 0.0075^\circ/\text{GHz}$ ), the frequency-swept bandwidths of 1.5 and 15 GHz (corresponding range resolution of 100 and 10 mm) give  $0.01^\circ$  and  $0.1^\circ$ , respectively. The former may be negligible, but the latter is comparable to one resolution point and must be suppressed. One idea for this is to use the combination of linear TO beam steering and sawtooth frequency shift. By setting their speeds appropriately, the beam shift is compensated and the step-like beam steering, suitable for LiDAR, is obtained.

## VII. CONCLUSION

We demonstrated the nonmechanical solid-state beam scanner based on the Si LSPCW slow-light waveguides and MZ switch trees, which were completely facilitated by the TO effect. It exhibited an angular range of  $40^\circ \times 8.8^\circ$ . Neglecting some of the points, which exhibited disordered spot profiles, the beam divergence was  $0.1^\circ$ , and the corresponding resolution points were  $400 \times 32 = 12,800$ . The response speed of this device was 70 kHz, for which the onset time was  $5.0 \mu\text{s}$ . If the response of the driver is fast enough, we could expect a frame-rate of 15 fps. The estimated insertion loss was 13 dB, at the lowest. Its reduction as well as the improved uniformity for efficient and high quality beam scanning are crucial issues toward the practical applications.

## REFERENCES

- [1] S. A. Khan and N. A. Riza, "Demonstration of 3-D wide angle laser beam scanner using liquid crystals," *Opt. Express*, vol. 12, no. 5, pp. 868–882, 2004.
- [2] G. R. B. E. Romer and P. Bechtoldb, "Electro-optic and acousto-optic laser beam scanners," *Phys. Procedia*, vol. 56, pp. 29–39, 2014.
- [3] K. Van Acoleyen, W. Bogaerts, J. Jägeršká, N. Le Thomas, R. Houdré, and R. Baets, "Off-chip beam steering with a 1-D optical phased array on silicon-on-insulator," *Opt. Lett.*, vol. 34, no. 9, pp. 1477–1479, 2009.
- [4] S. W. Chung, H. Abediasl, and H. Hashemi, "A monolithically integrated large-scale optical phased array in silicon-on-insulator CMOS," *IEEE J. Solid-State Circuits*, vol. 53, no. 1, pp. 275–296, Jan. 2018.
- [5] T. Kim *et al.*, "A single-chip optical phased array in a wafer-scale silicon photonics / CMOS 3D-integration platform," *IEEE J. Solid-State Circuits*, vol. 54, no. 11, pp. 3061–3074, Nov. 2019.
- [6] J. C. Hulme *et al.*, "Fully integrated hybrid silicon 2D beam scanner," *Opt. Express*, vol. 23, no. 5, pp. 5861–5874, 2015.
- [7] D. N. Hutchison *et al.*, "High-resolution aliasing-free optical beam steering," *Optica*, vol. 3, no. 8, pp. 887–890, 2016.
- [8] M. Zadka, Y. Chang, A. Mohanty, C. T. Phare, S. P. Roberts, and M. Lipson, "On-chip platform for a phased array with minimal beam divergence and wide field-of-view," *Opt. Express*, vol. 26, no. 3, pp. 2528–2534, 2018.
- [9] Y. Wang *et al.*, "2D broadband beamsteering with large-scale MEMS optical phased array," *Optica*, vol. 6, no. 5, pp. 557–562, 2019.
- [10] K. Shang *et al.*, "Uniform emission, constant wavevector silicon grating surface emitter for beam steering with ultra-sharp instantaneous field of view," *Opt. Express*, vol. 25, no. 17, pp. 19655–19661, 2017.
- [11] K. Kondo, T. Tatebe, S. Hachuda, H. Abe, F. Koyama, and T. Baba, "Fan beam steering device using a photonic crystal slow-light waveguide with surface diffraction grating," *Opt. Lett.*, vol. 42, no. 23, pp. 4990–4993, 2017.
- [12] X. Gu, T. Shimada, A. Fuchida, A. Matsutani, A. Ishimura, and F. Koyama, "Beam steering in GaInAs/GaAs slow-light bragg reflector waveguide amplifier," *Appl. Phys. Lett.*, vol. 99, no. 21, 2011, Art. no. 211107.
- [13] T. Baba, "Slow light in photonic crystals," *Nature Photon.*, vol. 2, no. 8, pp. 465–473, 2008.
- [14] T. Tamura, K. Kondo, Y. Terada, Y. Hinakura, N. Ishikura, and T. Baba, "Silica-clad silicon photonic crystal waveguides for wideband dispersion-free slow light," *J. Lightw. Technol.*, vol. 33, no. 14, pp. 3034–3040, 2015.
- [15] H. Abe *et al.*, "2-D beam-steering device using a doubly periodic Si photonic-crystal waveguide," *Opt. Express*, vol. 26, no. 8, pp. 9389–9397, 2018.
- [16] H. Ito *et al.*, "Wide beam steering by slow-light waveguide grating and prism lens," *Optica*, vol. 7, no. 1, pp. 47–52, 2020.
- [17] G. Takeuchi, Y. Terada, M. Takeuchi, H. Abe, H. Ito, and T. Baba, "Thermally controlled Si photonic crystal slow light waveguide beam steering device," *Opt. Express*, vol. 26, no. 9, pp. 11529–11537, 2018.
- [18] Y. Terada, K. Miyasaka, K. Kondo, N. Ishikura, T. Tamura, and T. Baba, "Optimized optical coupling to silica-clad photonic crystal waveguide," *Opt. Lett.*, vol. 42, no. 22, pp. 4695–4698, 2017.
- [19] J. Maeda, D. Akiyama, H. Ito, H. Abe, and T. Baba, "Prism lens for beam collimation in silicon photonic crystal beam-steering device," *Opt. Lett.*, vol. 44, no. 23, pp. 5780–5783, 2019.

**Takemasa Tamanuki** received the B.E. degree from the Faculty of Science, Tokyo University of Science, Tokyo, Japan, in 1988, and the M.E. and Ph.D. degrees from the Graduate School, Tokyo Institute of Technology, Tokyo, in 1990 and 1993, respectively, for his study on GaAs microcavity VCSELs. Since 1993, he has worked at NEC, OPTBAHN, Ibsiden USA R&D, and so on. Since 2019, he has been an R&D staff with Yokohama National University. He has studied and developed semiconductor lasers, telecom and datacom modules and sub-systems, and LiDAR devices.

**Hiroyuki Ito** received the B.E., M.E., and Ph.D. degrees from the Division of Electrical and Computer Engineering, Yokohama National University, Yokohama, Japan, in 2013, 2015, and 2019, respectively. Since 2019, he has been an R&D staff with Yokohama National University. He has studied Si photonics multi/demultiplexers based on coupled microrings, WDM transmitters including photonic crystal modulators, and slow-light LiDAR devices. He is a member of JSAP.

**Toshihiko Baba** (Member, IEEE) received the B.E., M.E., and Ph.D. degrees from Yokohama National University, Yokohama, Japan, in 1985, 1987, and 1990, respectively. He became an Associate Professor and then a Full Professor at Yokohama National University in 1994 and 2005, respectively. He has studied ARROW waveguides, VCSELs, microdisk lasers, photonic crystals (PCs), and Si photonics. He has demonstrated PC-based devices such as slow-light waveguides, high-speed modulators, beam scanners, nanolasers, biosensors and LEDs. He also fabricated various Si photonics components including the first arrayed waveguide grating. He is a member of JSAP, IEICE, and OSA, as well as an Associate Member of the Science Council of Japan. He served as a Vice President of JSAP from 2018 to 2020. He was the recipient of the JSPS Award in 2005, the IEEE/LEOS Distinguished Lecturer Award in 2006/2007, the Ichimura Academic Award in 2012, and the Education, Culture, Sports, Science Minister's Commendation in 2016.